Applied Physics A (2021) 127:118
https://doi.org/10.1007/s00339-020-04162-5

Applied Physics A
Materials Science & Processing

Surface plasmon resonance based highly sensitive gold coated PCF biosensor

Mohammad Rakibul Islam[1] · A. N. M. Iftekher[1] · Kazi Rakibul Hasan[1] · Md. Julkar Nayen[1] · Saimon Bin Islam[1] · Rakina Islam[1] · Raisa Labiba Khan[1] · Ehtesam Moazzam[1] · Zarrin Tasnim[1]

Received: 24 September 2020 / Accepted: 21 November 2020

Abstract
A highly sensitive surface plasmon resonance-based PCF biosensor is explored in this research work. Outside the fiber frame, active plasmonic material gold (Au) with a thickness of 25 nm has been deposited which is chemically steady and is the primary sensing layer of the presented sensor. Unknown analytes could be detected by being flown on the metal surface or leaked onto the metal layer's outer surface. In this paper, we used circular airholes for external sensing of the unknown analyte. The suggested sensor obtains the maximum wavelength sensitivity of 14,500 nm / RIU in X-polarization mode and the maximum amplitude sensitivity of 4738.9 RIU^{-1} for Y-polarized mode, respectively in the spectrum of 1.35–1.41 for the analyte refractive index (RI). The lowest wavelength sensor resolution offered by this sensor is 6.9×10^{-6} RIU and the lowest amplitude sensor resolution is 2.11×10^{-6} RIU for Y-polarized mode with FOM of 387 and 364 for X and Y polarization. In the presence of a perfectly matched layer (PML), the sensing output of the presented sensor is analyzed using the finite element method (FEM) based software named COMSOL Multiphysics version 5.3a. From our simulation result, it is important to note that the proposed sensor demonstrates a noteworthy sensor performance for both polarization modes so that the choice of light sources during the practical implementation is more frequent. The findings also show some bright features that our proposed sensor can detect organic chemicals, biochemical analytes and can also be used in medical diagnostics immensely.

Keywords Surface plasmon resonance · Optical fiber sensors · Photonic crystal fiber · Sensitivity · Resolution

1 Introduction

Surface plasmon resonance (SPR) phenomenon has achieved tremendous admiration in the field of bio-sensing applications, food controlling, medical technologies, chemical and physical sectors etc. due to its vast characteristics**.** Surface plasmons are surface charges that are constructed due to propagation of confined electromagnetic (EM) field along with the interface between a metal and dielectric after an electric oscillation took place immensely. The evanescent field is located at metal–dielectric interface significantly because of the exponentially decaying electrons that result under a shaft of light. Kretschmann configuration is another operable configuration in which with a glass prism, light is focused onto a metal film and the subsequent reflection is sensed. This configuration detects collective oscillations of free electrons which are called surface plasmons. The light intensity or electromagnetic field changes if samples are present and optical sensors are associated with this occurrence. Because of their availability to attain small portability, high detection, integrated capacity, compatibility and so on, multiple methods like Sagnac-interferometer, long-distance microstructures sensor, engraved oblique Bragg fiber gratings, SPR etc. have been implemented to improve fiber biosensor performance [1]. Optical sensor is defined as an advanced device capable of converting light rays to electrical signals so that the ambient state changes or response can be detected, or electromagnetic wave intensities can be measured. There are various sensing techniques such as resonant mirrors, SPR, photoluminescence, micro-ring resonator, evanescent wave absorption spectroscopy and so on. Among these SPR-based biosensor is the most promising one as it has compact sensing features and innovative ability of detection criteria in nature [2]. First, Liedbarg et.al investigated

✉ Mohammad Rakibul Islam
rakibultowhid@yahoo.com

[1] Department of Electrical and Electronic Engineering, Islamic University of Technology, Boardbazar Gazipur-1704, Bangladesh

Published online: 19 January 2021

prism-coupled SPR for detecting chemical gas and bio-sensing approaches [3, 4]. A prism-based SPR sensor presents some restrictions such as being bulky and having remote sensing even though it is cheaper and easily available [5, 6]. To overcome these obstacles, SPR sensors based on PCF applications have been introduced. SPR sensor based on PCF is the composition between the science of plasmonics and technology regarding PCF [7]. Evanescent field is generated through the core-cladding region due to light propagation. Evanescent field penerates the cladding region of the sensor structure hitting the plasmonic metal surface that will excite the metal surface's free electrons. These excited electrons begin resonating when the balance between the frequencies of free electrons and an incident photon is established. At this condition, on the metal–dielectric interface, surface plasmon wave is produced which is known as resonance state. A sharp loss peak with the adjacent dielectric layer of metal sheet occurs at this resonance condition which is very sensitive. In the real region of the surface area component of the active Surface Plasmon Polariton (SPP), variations in analyte refractive index (RI) will cause a subsequent variation in index, resulting in a change in the corresponding phase or resonant wave frequency. Through measuring this change in resonant wavelength, particles and molecules are observed. This is the basis of PCF SPR's operating theory [8, 9]. The SPR phenomenon was observed experimentally by introducing the manufacturing of gold nanowire with PCF for the first time by M. A. Schmidt et al. [10]. Due to the flat PCF structure, compared with the external sensing approaches D-shaped structure gives additional efficiency by the use of analogous metal. Among the two sensing techniques (Internal and external), external sensors are highly appreciable due to the connection of analyte to the outer surface of PCF. But it requires precise polishing which provides a challenge in this method for extracting a portion of PCF. A symmetrical D-shaped SPR sensor based on PCF was reported by Chao et al. having amplitude sensitivity of 1222 RIU^{-1} and wavelength sensitivity of 14,660 nm/RIU [11, 12]. From recent reports, we found another one by Rahman et al. who designed a D-shaped structure effectively having a wavelength sensitivity of 3000 nm/RIU and AS of 241 RIU^{-1} [13]. T. Huang et.al in this field found a larger WS of 6000 nm/RIU and AS of 148 RIU^{-1} [14]. Outside the PCF structure there lays a plasmonic metal coating which facilitates external sensing methods, highly desirable for real-time environmental tracking systems. Highest sensitivity of 5,500 nm/ RIU was also found by averaging the results of researchers investigating two-sided based SPR sensors for detecting the lower RI in mid-infrared region [15]. To aid in more feasible and simple fabrication, this technique has gained much popularity in recent years. PCF has shown great potential to control evanescent field penetration by having noteworthy characteristics such as single-mode propagation, compact size, simpler launching of the light, and ability to control and proved itself as a contender for SPR sensor. In general silver, copper and gold are the materials that are used in sensor designed with SPR phenomenon. In our paper, we used Gold (Au) as a novel plasmonic material which shows reliability due to its chemical stability. Gold can also provide with large resonance wavelength shift [9]. Rifat et al. investigated a gold-coated sensor and achieved maximum WS of 11,000 nm/RIU and AS of 1420 RIU^{-1} [7]. It can retain its stability even in aqueous state. On the contrary, compared to gold, silver can provide sharper resonance peak and little to none interband transition. But oxidation of silver in the humid environment results in a reduction of the accuracy of analyte identification [16]. This is why theoretical works and experiments are done using gold as the plasmonic medium [17, 18]. To minimize the oxidization level, nowadays a thin graphene layer or Tio2 is also applied with the above-mentioned materials for getting better sensing performance [19, 20]. Using Au-TiO2 as the bimetallic layer for the analyte channel, some researchers found a maximum sensitivity of 25,000 nm/RIU [21]. To date, majority of the PCF SPR sensors proved that one of the polarization modes is stronger than the other. All polarization modes also have the same resonant wavelength coupling [1]. There have been a very small number of dual-polarized PCF SPR sensors that denote equal sensitivity in both polarized modes. Y-polarization has been shown to provide more evanescent field and surface excitation in earlier work due to the complex design, micro-sized airholes and so on. Another form of SPR termed as LSPR also got much popularity recently which could combine both waveguiding and plasmonic resonance technique [22]. In this paper, we are proposing a simple dual-polarized, highly sensitive gold-coated PCF-based SPR sensor having circular-shaped airholes for gaining better sensing performance and low loss. The sensor which is proposed can provide low losses and high sensitivity which is numerically tested by the Finite Element Method (FEM) through the software COMSOL 5.3a that is available to us commercially. Our goal is to successfully design a sensor that is structurally simple, easy to fabricate giving high sensing performance. Our desired characteristics also count for low loss, high sensor resolution with improved WS and AS. The simplicity of design allows for a practically realizable PCF manufacturing that provides the possibility of commercial use of the sensor.(Fig. 1, 2).

According to the mathematical explanation, resonance occurs when the real effective refractive index (n_{eff}) of core-guided mode and surface plasmon polaritons (SPP) mode value are exactly the equal. The core mode's effective value of the refractive index (RI) intersected with that of SPP mode at RI = 1.4549 and at the corresponding lambda = 625 nm the peak loss occurred. So resonance will occur at lambda = 625 nm. Unknown analyte will be detected

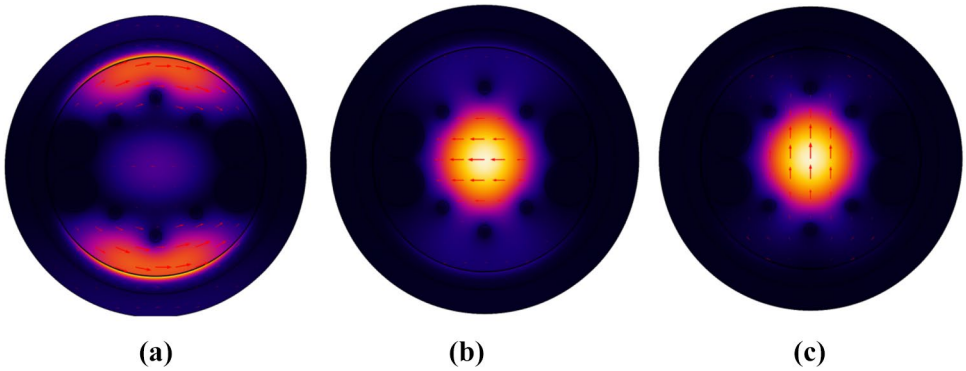

Fig. 1 **a** SPP-mode, (**b**) core-guided mode X-polarization, (**c**) core-guided mode Y-polarization

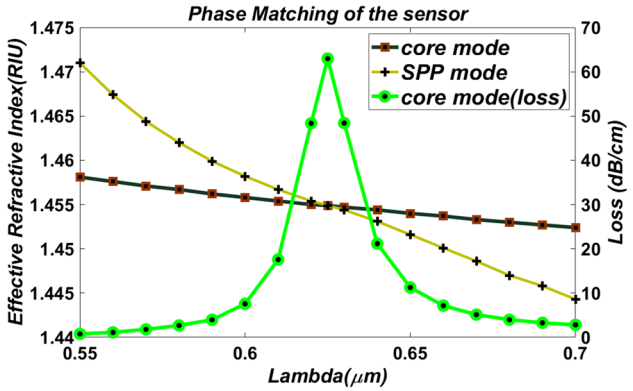

Fig. 2 Phase matching of core guided mode and SPP mode

at this phase of matching wavelength by shifting the resonance peak.

2 Design methodology

The design is completed and investigated using the commercially available COMSOL 5.3a software. The method which has been used for designing the sensor is the stack and draw method. Finite Element Method (FEM) was applied to assess the sensor. Figure 3 denotes the different parts of the sensor. The structure has been computationally analyzed with 153,001 degrees of freedom and mesh of "Extra Fine" was appointed for the simulation of the structure. Complete mesh consists of 34,552 domain elements and 2358 boundary elements. Meshing of the structure gives us finite solutions instead of infinite solutions and is crucial for solving through FEM. The values of various parameters in the design are decided upon their sensing performance. The material used in the perfectly matched layer (PML) and in the surface on which air holes reside is Silica. The refractive index of Silica ($n(\lambda)$) has been calculated using the Sellmeier Eq. (1) [23, 24]

$$n^2(\lambda) = 1 + \frac{B_1\lambda^2}{\lambda^2 - C_1} + \frac{B_2\lambda^2}{\lambda^2 - C_2} + \frac{B_3\lambda^2}{\lambda^2 - C_3} \quad (1)$$

where silica's RI is n, λ is the wavelength in μm. The Sellmeier coefficients were taken from [24].

$B_1 = 0.6961663$, $B_3 = 0.8974794400$, $C_1 = 4.67914826 \times 10^{-3}\,\mu m^2$, $C_2 = 1.35120631 \times 10^{-2}\,\mu m^2$, $C_3 = 97.9340025\,\mu m^2$

Figure 3 a shows various layers of the sensor and their materials. b shows the realization of the air holes through the stacking of capillary rods. The scaled down air holes are represented by capillaries with thick wall and the greater

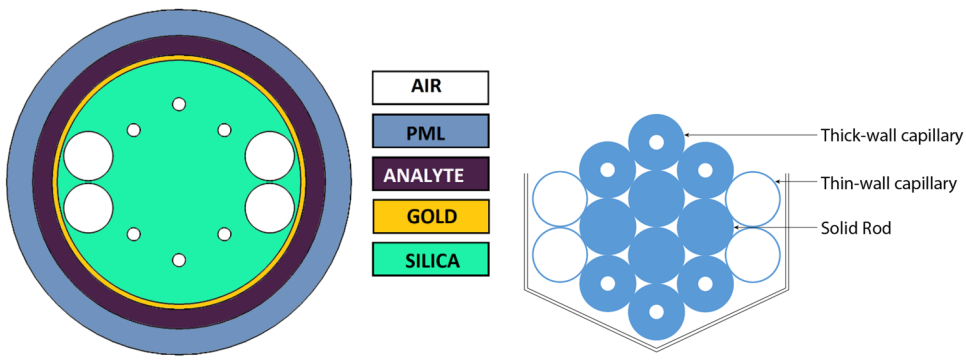

Fig. 3 **a** 2-D cross-sectional view and (**b**) stacking the proposed sensor

air holes are depicted by capillaries with a thin wall. Solid rods have been inserted where there is no air hole [25]. This stacking ascertains the practicality of realizing the fabrication of the designed sensor (Fig. 4).

3 Investigation of sensing performance of parameters

The sensor performance can be considered as a function of the geometrical parameters of the PCF. Moreover, these parameters affect the interaction of the gold surface and the evanescent field. Thus, these parameters must be selected carefully. These parameters include gold film thickness, analyte layer thickness, PML layer thickness, bigger air hole diameter, and smaller air hole diameter and refractive index values. Initially we used Gold film thickness = 30 nm, Analyte layer thickness = 0.96 µm, PML layer thickness = 1.5 µm, Bigger air hole diameter = 0.95 µm, Smaller air hole diameter = 0.25 µm, RI = 1.4 before optimization.

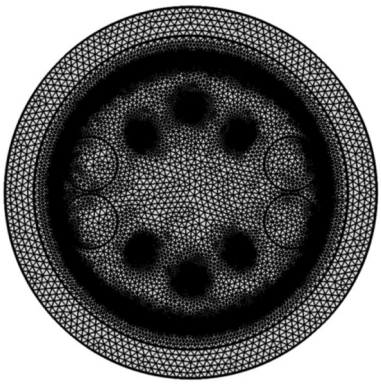

Fig. 4 Mesh structure of the proposed sensor

While optimizing these parameters, we measured the confinement loss (CL), amplitude sensitivity (AS), and wavelength sensitivity (WS) for different values of any particular parameter.

i) Before optimizing the other parameters, we will talk about the inner circle of the gold layer in the structure. Its radius is kept at 4.7 µm. If it is increased, amplitude sensitivity would be decreased dramatically. Now let us examine the gold layer's thickness at first. Gold is used as a chemically stable and active plasmonic material in the aqueous region in this sensor design. It enhances the detection level of an analyte in the sensor. Proper thickness of gold layer contributes to enhanced sensor performance and affects the shift in resonant wavelength. Gold provides a significant resonance peak shift, which can be seen from Fig. 5a. Apart from this, the Gold layer also provides fabrication feasibility. Upon investigating, it was found that an increase in thickness caused the resonance peak to shift towards the larger wavelength. The gold layer's RI was measured using Drude-Lorenz model which is given by Eq. (2) [23, 26].

$$n_g^2 = \varepsilon_\infty - \frac{w_D^2}{w\left(w + j\gamma_D\right)} + \frac{\Delta\varepsilon^2\rho}{\left(w^2 - \rho^2\right) + j\tau w} \tag{2}$$

where n_g= gold's refractive index, ε_∞= 5.9673 is gold's permittivity, $\Delta\varepsilon$= 1.09 is the weighting vector, w is the angular frequency of the guided light, w_D and γ_D are the plasma frequency and damping frequency respectively, where $w_D/2\pi = 2113.6$ THz, and $\gamma_D/2\pi = 15.92$ THz. Moreover, ρ and τ indicate the frequency and spectral width of the Lorentz oscillator where $\rho/2\pi = 650.07$ THz and $\tau/2\pi = 104.86$ THz

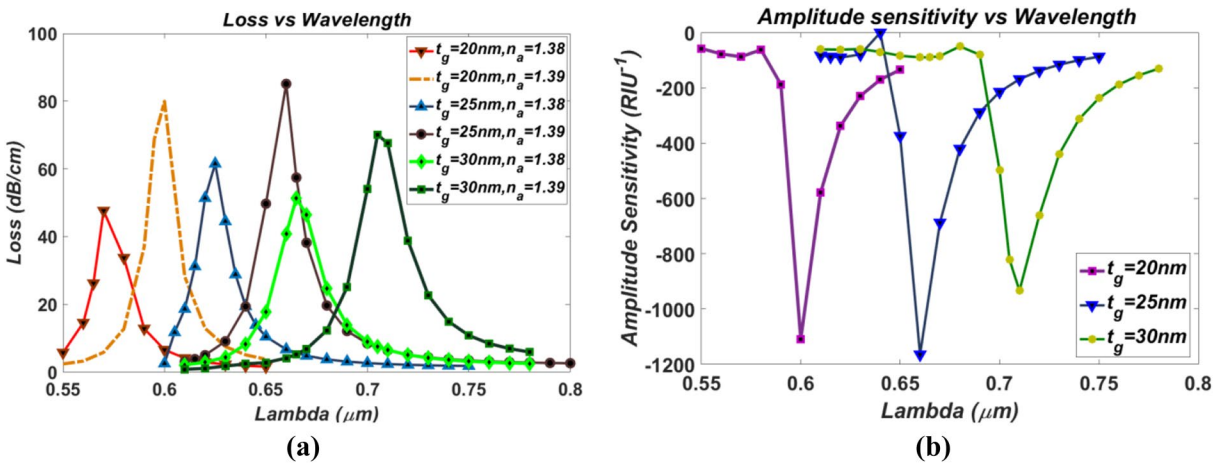

Fig. 5 **a** Loss vs. Wavelength and (**b**) Amplitude Sensitivity vs. Wavelength for various thicknesses of gold

[23, 26]. Nanoscale properties of gold are crucial for the surface plasmon waves (SPW) to appear. But this fact applies for thickness between 20 to 50 nm [27, 28]. The value of gold thickness was the first parameter to be optimized. Thus to do so, all the other settings were kept constant, and gold thickness was varied from 20 to 35 nm, and the range of wavelength was [550–800 nm]. After comparing the results, we obtained amplitude sensitivity at various gold thickness values by amplitude interrogation method. From Fig. 5a, b, it is evident that loss at gold thickness = 25 nm is maximum, and a maximum sensitivity (1164 RIU^{-1}) was found at gold thickness = 25 nm. It can also be followed that the amplitude sensitivity at thickness = 20 nm is higher than the sensitivity obtained at thickness = 30 nm. Thus we take gold thickness = 25 nm as the optimized value for this design.

The confinement loss was calculated from the expression (3) [29].

$$\alpha_{loss} = 8.686 \times 2\pi/\lambda \times I_m\left(n_{eff}\right) \times 10^4,\ dB/cm \tag{3}$$

where $2\pi/\lambda$ indicates wave number in the free space and the operating wavelength, λ is in µm [23, 29, 30]. From the simulation, we can deduct the value of Im(neff) which signifies the imaginary part of the effective index [26]. We are optimizing all the parameters considering the amplitude sensitivity since it is a simple and economic process [29–31] and wavelength interpolation is not required in this case. In the wavelength interrogation method, the maximum resonance wavelength shift can give the sensitivity of a sensor. Wavelength sensitivity was formulated by the wavelength interrogation method through the formula (4) [23, 29, 32].

$$S_w(\lambda) = \frac{\Delta\lambda_{peak}}{\Delta n_a} \tag{4}$$

where, $\Delta\lambda_{peak}$ is the difference between the resonant wavelengths and Δn_a is the difference between analyte RI. The amplitude sensitivity can be obtained by the following Eq. (5) [23, 33].

$$S_A(\lambda) = -\frac{1}{\alpha\left(\lambda, n_a\right)} \frac{\Delta\alpha\left(\lambda, n_a\right)}{\Delta n_a} \tag{5}$$

Here $\alpha(\lambda, n_a)$ is the overall loss where analyte refractive index is equal to n_a and $\Delta\alpha(\lambda, n_a)$ is the difference between two adjacent loss spectra due to a small change in the refractive index of the analyte, Δn_a is the change of the refractive index of the anlayte [26, 33]. Amplitude sensitivity rises with an increment of analyte RI and peak point shifts towards higher wavelength.

ii) Optimization of analyte thickness:

Mode confinement and total reflection are enabled by the difference in the analyte refractive indices [23, 27, 33]. This sensor is based upon the unknown analyte detecting performance. Thus, analyte thickness is a crucial part of the design. After getting the optimized value of gold thickness, the value of analyte thickness was optimized by keeping the gold thickness parameter constant and varying the analyte thickness. Few factors were considered during optimizing the thickness. A thinner analyte layer produces better results regarding sensitivity. But detection of analyte using a layer too thin or too thick would result in errors. The resulting loss and sensitivity at different analyte thicknesses are shown in Fig. 6. As the values were varied, it was found that at a thickness of less than 0.8 µm, the amplitude sensitivity decreased. A similar case was observed for the thickness values of more than 0.8 µm, which is evident from Fig. 6b. At thicknesses lesser than 0.5 µm, AS of more than that of 0.7 µm were found. Due to the lack of practicality of the thickness, those thicknesses were not chosen. Thus the values were varied from 0.7 µm to 1 µm, and the wavelength was varied from 550 to 750 nm. At the thickness of 0.8 µm, the highest sensitivity of 1214 RIU^{-1} was found. Hence this value was made the optimum value for analyte thickness.

iii) Optimization of PML (Perfectly Matched Layer) thickness:

Perfectly Matched Layer (PML) is an integral part of the simulation even though its absence in practice does not result in an erroneous result. Its capacity is to assimilate the dissipated waves from PCF and in this manner, it behaves as a computational boundary [22, 23]. The difference in qualities due to the variation of the thickness of the PML is seen in Fig. 7. The confinement loss, as appeared in Fig. 7a, show that PML has an insignificant effect on the confinement loss of the sensor in contrast with the loss acquired for the analyte case (Fig. 6a). When the PML thickness is made under 1.5 µm, the Amplitude sensitivity decreases, and a similar case happens for a thickness of more than 1.5 µm. Taking the detecting performance and size of the sensor into thought, we pick 1.5 µm (ranging from 0.9 µm to 2 µm) as the ideal PML thickness, where maximum sensitivity (1245 RIU^{-1}) has been found.

iv) Optimization of bigger air hole diameter:

In this design, inside the first inner circle, there are air holes of two sizes. Subsequent to advancing the thickness of the gold, analyte, and PML layers, we optimized the radius of bigger airholes between two different airholes. Figure 8 depicts the variety of confinement loss

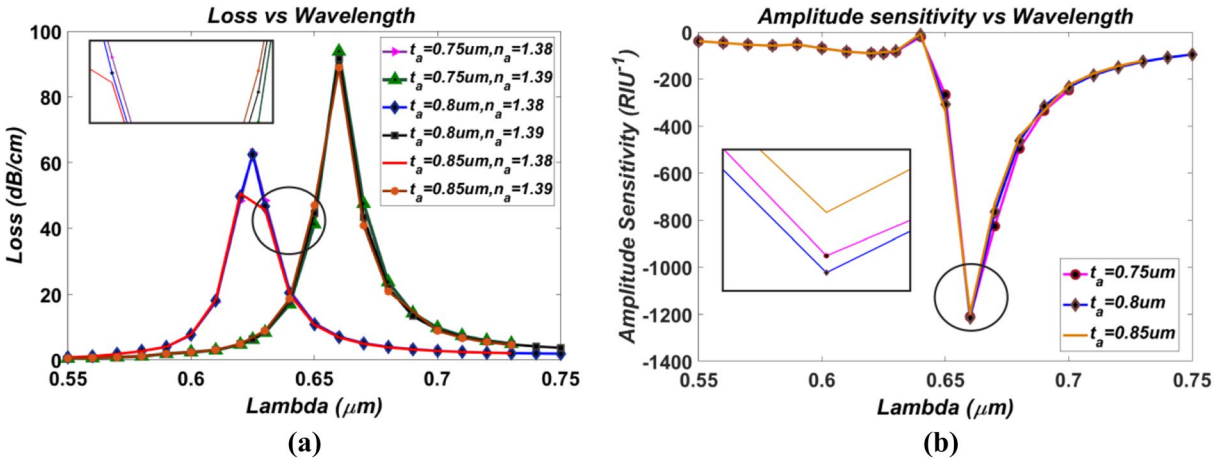

Fig. 6 **a** Loss vs. Wavelength for different analyte thicknesses and (**b**) Amplitude Sensitivity vs. Wavelength for different Analyte thicknesses

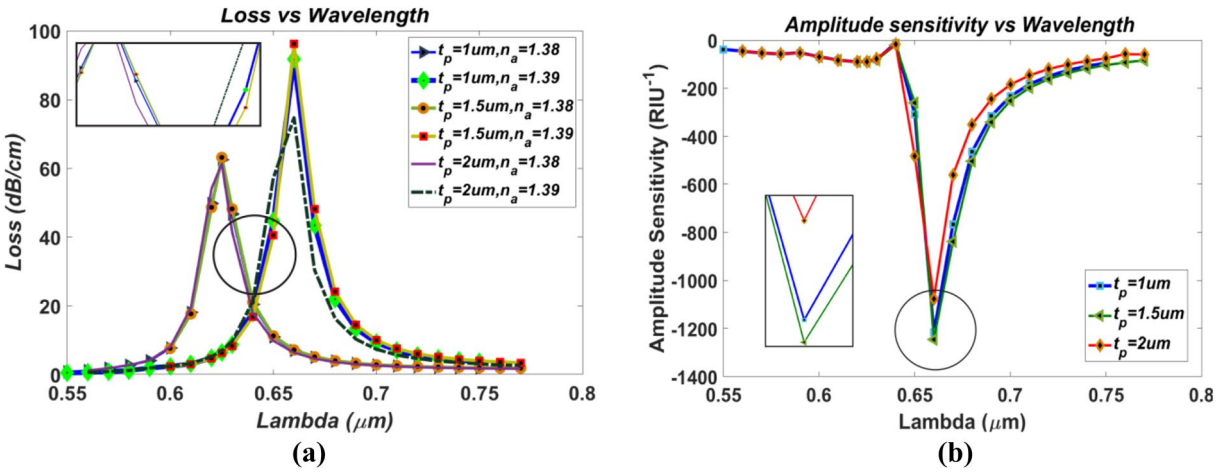

Fig. 7 a Loss vs. Wavelength for different PML thicknesses and (**b**) Amplitude Sensitivity vs. Wavelength for different PML thicknesses

of the sensor, for change in range of greater airhole. The Refractive index of the core guided mode is influenced by the changes in the airholes and thus influences the phase matching between SPP mode and the core guided mode. Changes in the resonance intensity, resonance peak and the resonance wavelength are seen because of this. Subsequently, we can change the size of this airhole to optimize sensor performance. We found maximum sensitivity of 1271 RIU^{-1} at radius = 0.852 μm while varying the radius from 0.75 μm to 1 μm in the wavelength interval of 550 nm–800 nm. It can be seen that changing the radius of the bigger airhole did not result in a significant amount of change in confinement loss and sensitivity. Positioning of the airholes of this radius and contribution to producing SPW are the reasons behind this [23, 33].

v) Optimization of smaller air hole diameter

Between the two different radii, now the smaller one is being optimized. In the cladding region the air holes radius plays an essential part in sensing performance. These airholes play a bigger role in producing the surface plasmon polaritons and waves. Thus the effect of changing their radius by small amount is significant on confinement loss and Amplitude sensitivity [23, 33]. From Fig. 9, we can see that the radius of this air hole mostly affects the confinement loss. The highest loss, in this case, is much higher than the highest loss obtained in the previous cases. With the increment in diameter, the core guided useful index will diminish and guiding light will spread out over the cladding region. This will result in the reduction of surface excitation. Thus choosing a proper optimum radius for the air holes of this position is a very crucial investigation to perform.

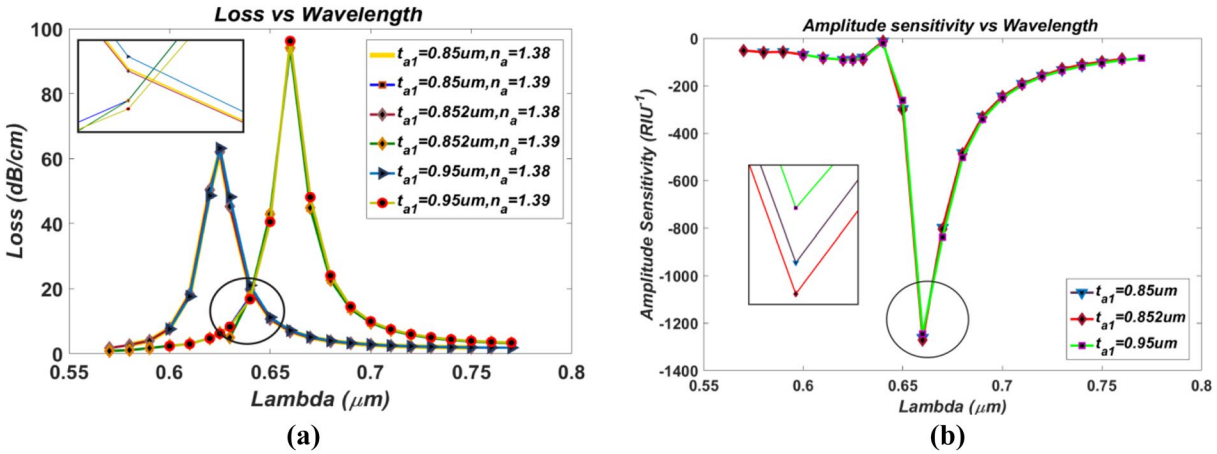

Fig. 8 **a** Loss vs. Wavelength for different radii and (**b**) Amplitude Sensitivity vs. Wavelength for different radii

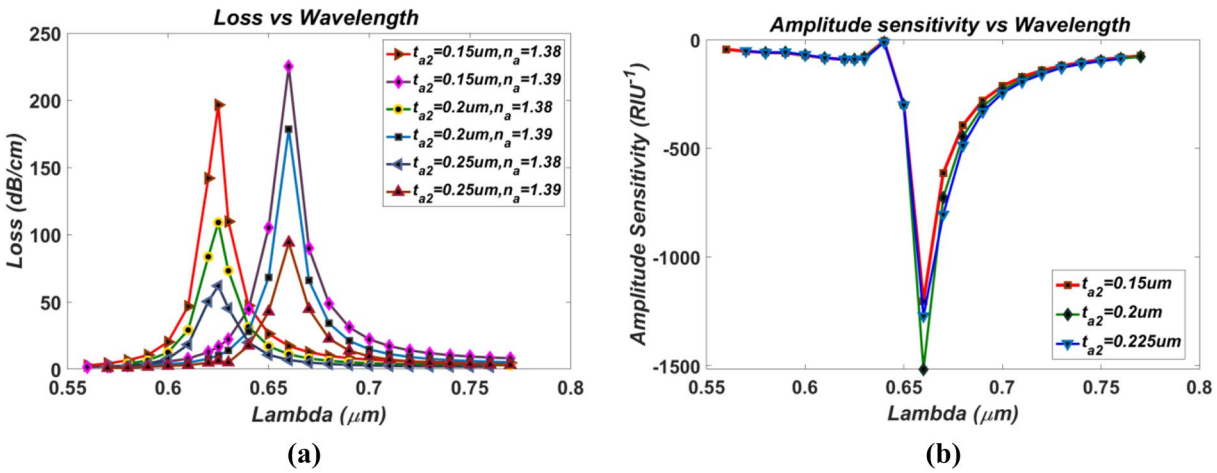

Fig. 9 **a** Loss vs. Wavelength for different radii and (**b**) Amplitude Sensitivity vs. Wavelength for different radii

After obtaining the optimized value of the bigger radius, the value of a smaller radius was varied from 0.15 µm to 0.3 µm in the wavelength interval of 550 nm—800 nm. The maximum sensitivity of 1515 RIU^{-1} was found at 0.2 µm among the other values, and it is evident in Fig. 9b. Excitation is a pivotal issue for SPR. In Fig. 9a, the confinement losses of core guided mode found at different radii of this air hole are expressed.

vi) Sensing performance for different RI (Refractive Index) values:

Between X-polarization and Y- polarization modes, Y- polarization generates larger evanescent field exciting more surface-free electrons in the loss curve. It is better than X-polarization even though similar properties can be found in X-polarization. That is why for the final result, we are considering y-polarization as the fundamental mode. Within the wavelength range between 520 and 820 nm, the characteristics of confinement loss and amplitude sensitivity for the Y polarization of the analyte RI varying from 1.35 to 1.41 are demonstrated in Fig. 10a, b. Confinement loss characteristics of different analytes provide the performance measurement of the sensor. An increament of analyte RI is shown in Fig. 10a which states that the resonance peak shifts towards the longer wavelengths eventually. It is observed from the Fig. 10 that this instance results in high sensitivity for greater RI. Figure 11 describes the characteristics of the pattern or behavior of the confinement loss and amplitude sensitivity with the change of analyte RI. Both the parameters follow a quadratic behavior which results in a sharp increase in their values at the last RI of our range. We found a resonance wavelength shifting of 80 nm for the analyte RI of 1.40 and 1.41 in Y polarization mode

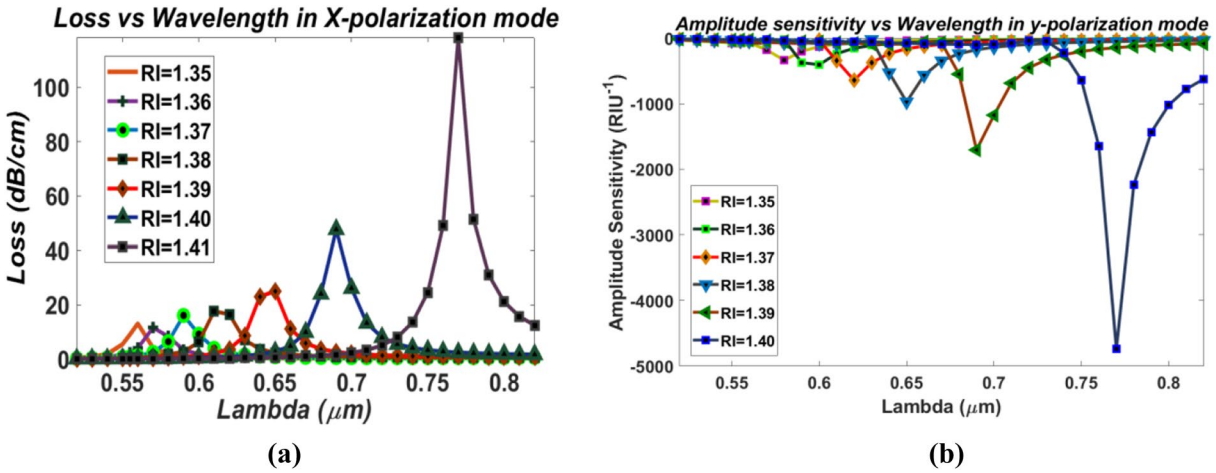

Fig. 10 **a** Loss vs. Wavelength for different RI and (**b**) Amplitude Sensitivity vs. Wavelength for different RI

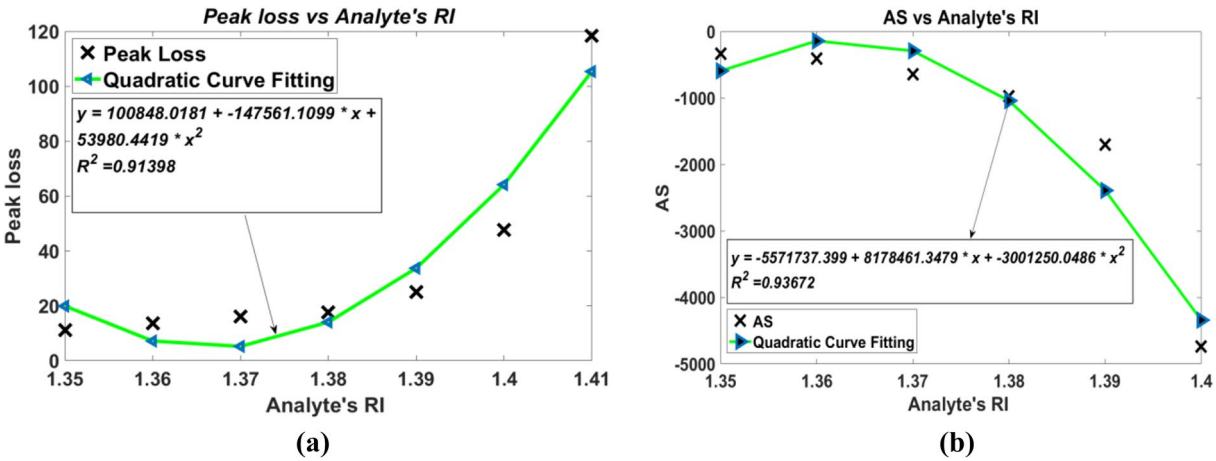

Fig. 11 Polynomial behavior of (**a**) peak loss and (**b**) amplitude sensitivity at different RI

after investigating Fig. 10a which is the maximum in this case. At RI of 1.4 in the Y polarized mode, we achieved a wavelength sensitivity of 8000 nm/RIU which is the maximum one. For X polarized mode, a maximum shift of 145 nm was found and thus a maximum wavelength sensitivity of 14500 nm/RIU was found in that mode.

For detecting the analytes, the amplitude (phase) detection method is more convenient than the wavelength interrogation method. The amplitude sensitivity which we calculated for y polarization mode has appeared in Fig. 10b. As sharper loss peak is obtained at analyte RI = 1.4, the maximum amplitude sensitivity for the Y polarization is evidently 4738 RIU^{-1}. At wavelength 690 nm, the maximum amplitude of the loss spectrum is 118 dB/cm and the maximum wavelength sensitivity equals to 14,500 nm/RIU are achieved for analyte refractive index = 1.4 at X-polarized mode (Fig. 11).

vii) Fiber Linearity

To get an optimized sensor within a defined effectual range, linear fitting features are needed. For the measurement of sensors, high sensor linearity is a precondition particularly for high RI analytes. From the slope of the linear fitting curve, the average sensitivity of the proposed sensor is depicted. The nonlinearity of the reaction causes critical varieties in the average sensitivity and resolution making the detection procedure increasingly intricate. Thus it is not a desired quality in a sensor [26, 30, 34]. If the sensor shows linearity, it is easier to predict the resonant wavelength for the higher analyte

RI [9]. The more the linearity, the more proportional is the shift of resonant wavelength. The correlation coefficient (R) can depict the linearity and it is acquired by performing linear regression. As a component of analyte RI, linear fitting of the resonant wavelength is portrayed in Fig. 12.

The regression equation for the linear fit of the proposed sensor is $y = -3949.2857 + 3321.4286x$ and Regression Co-efficient is $R^2 = 0.90927$. For the quadratic fit, the equation and value of R^2 were found to be $y = 107117.3838 - 157678.5755x + 58333.3348x^2$ and 0.99341. It is evident that the value of the correlation coefficient is very close to the value 1. This shows the continuous response over the sensing region of 1.35–1.41.

From Fig. 12, it was found that a quadratic fit produced a closer regression coefficient to 1 than that of a linear fit. From this instance, the sensor performance can be predicted for the next RI range following the quadratic behavior.

viii) Sensor resolution

The suitability and importance of a sensor not only rely upon a higher sensitivity but also relies upon precise detection of the minimum spectral shift change, which detects analytes properly. By investigating the sensor resolution, small changes of the spectral shift with precision can be identified effectively. In the interval of 1.35–1.41, the analyte refractive indexes are shown. An average shift of 49.16 nm and 35 nm in the resonance wavelength is observed with the variation of 0.01 in the refractive index for X and Y polarized mode, respectively. From this phenomenon, we obtained an average spectral sensitivity of 3500 nm/RIU accurately. In resolution wavelength interrogation method, resolution is calculated by the Eq. (6)

$$R(w) = \frac{\Delta n_a \times \Delta \lambda_{\min}}{\Delta \lambda peak(RIU)} \tag{6}$$

and our result is compared with the reference [35]. While producing practical simulation, Optical Spectrum Analyzer (OSA) is used. To correctly assess the change in resonant wavelength shift for the smallest change, this instrument computes results with a wavelength resolution of 0.1 nm or 1 Å [36]. Assuming that, $\Delta\lambda_{min} =$ 0.1 nm which denotes the minimum spectral resolution, maximum peak shift denoted as Δλ peak and the analyte RI change is $\Delta n_a = 0.01$, we can calculate the maximum sensor resolution [9]. The amplitude detection procedure is proved as a very cost-effective method to measure sensitivity. The absence of the need for spectral manipulation reduces the number of iterations done for calculation [21]. The resolution determined by the amplitude interrogation method is calculated by the Eq. (7)

$$R(A) = \frac{\Delta n_a}{S_A(\lambda)} \tag{7}$$

Here Δn_a=0.01 and $n_a(\lambda)$ is the amplitude sensitivity. Amplitude sensitivity is appeared in Fig. 10b as a function of analyte RI. From Fig. 10b, among the refractive indexes of 1.35, 1.36, 1.37, 1.38, 1.39, 1.4 respectively, we obtained amplitude sensitivities and a maximum sensitivity of 4738.9 RIU^{-1} is achieved for the analyte refractive index of 1.4 in our case. Thus, the lowest amplitude sensor resolution it can offer is 2.11 $\times 10^{-6}$ RIU. This Amplitude Sensitivity is taken as the final result from our proposed sensor which is the best result it can produce to its capabilities.

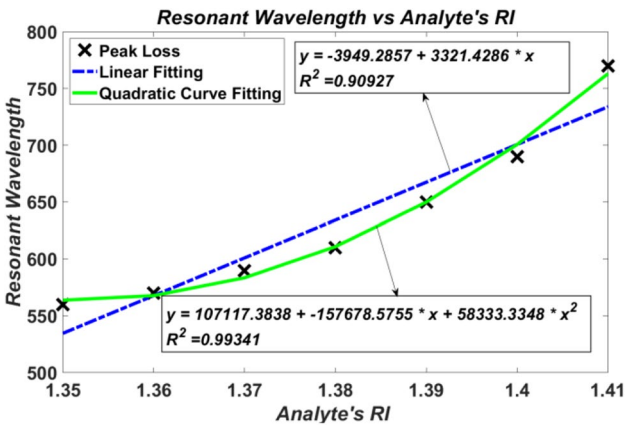

Fig. 12 Resonant wavelength vs. analyte RI for Y-polarization

ix) Figure of Merit

Another parameter which can describe the quality of the sensor is the Figure of Merit (FOM). FOM is characterized as the proportion of wavelength sensitivity and FWHM (Full Width at Half Maximum) which is given below in Eq. (8)

$$FOM = \frac{S_w(\lambda)}{FWHM} \tag{8}$$

A better estimation of FOM is finalized when the sensitivity is high and FWHM is low [24, 30]. The FWHM obtained at refractive index of 1.35, 1.36, 1.37, 1.38, 1.39, 1.4, 1.41 are 23, 15, 20, 25, 20, and 37.5 for x-polarization respectively. The FWHM obtained at refractive index of 1.35, 1.36, 1.37, 1.38, 1.39, 1.4

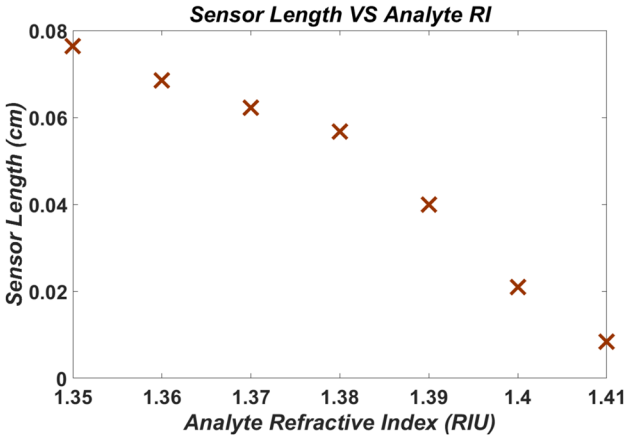

Fig. 13 Sensor length at different Refractive Indices of Analyte RI

and 1.41 are 18, 20, 20, 27, 28 and 22 respectively for y-polarization.

x) Sensor Length

Sensor length is required to determine the power detected by the sensor at the output for an input power. It can be computed by taking the inverse of the maximum confinement loss found in cm at each RI which is given in Eq. (9) [37].

$$L = \frac{1}{\alpha\left(\lambda, \Delta n_a\right)} \tag{9}$$

Figure 13 depicts the sensor lengths at different analyte RI. Since it is inversely proportional to the confinement loss, the minimum loss gives the maximum sensor length applicable to the sensor.

Table 1 signifies the performance analysis of the proposed sensor. In this table, we can see, with increasing RI, resonant peak shifts to the right just as our discussion in theory. In Table 2, the correlation of performance of this sensor has been made with different reported sensors and the superiority of this proposed sensor has been established.

4 Conclusion

A novel highly amplitude sensitive gold-coated SPR sensor based on PCF, has been redesigned and researched to detect three types of analytes that are- organic, biochemical, and biomedical. In depth analysis and numerical simulation of the sensor exhibits optimum wavelength sensitivity specifically for X polarization that is about 14,500 nm/ RIU and the maximum amplitude sensitivity of 4738.9 RIU^{-1} and the lowest amplitude sensor resolution of 2.11 $\times 10^{-6}$ RIU for Y-polarization mode, respectively in the range of 1.35 to

Table 1 Performance analysis of the proposed sensor

Analyte RI	Peak Loss(dB/cm)	Resonant Peak Wavelength(nm)	Resonant Peak Shift(nm)	Amplitude Sensitivity(RIU^{-1}))	Wavelength Sensitivity(nm/RIU) In X-polarization	Wavelength Sensitivity(nm/RIU) In Y-polarization	FWHM (X-pol)	FWHM (Y-pol)	FOM(X-pol)	FOM(Y-pol)
1.35	13.08	560	10	336.5	2000	1000	23	18	86	55
1.36	14.59	570	20	404.908	2000	2000	15	20	133	100
1.37	16.08	590	20	643.45	2500	2000	20	20	125	100
1.38	17.63	610	40	971	3500	4000	25	27	140	148
1.39	25.01	650	40	1705	5000	4000	20	28	250	143
1.4	47.68	690	80	4738.9	14,500	8000	37.5	22	387	364
1.41	118.4	770	N/A	N/A	N/A	N/A	12.5	10	N/A	N/A

Table 2 Performance comparison with reported sensors

Ref. No	Structure type	RI-range	Polarization mode	Amplitude sensitivity (RIU^{-1})	Wavelength sensitivity (nm/RIU)	Resolution (Wave. Int.) (RIU)	Resolution (Amp. Int.) (RIU)
[21]	A Hi-Bi ultra sensitive SPR	1.33–1.38	N/A	1411	25,000	4.00×10^{-6}	7.09×10^{-6}
[22]	Localized SPR biosensor	1.33–1.43	N/A	2050	111,000	9×10^{-6}	4.88×10^{-6}
[7]	Propagation controlled photonic crystal fiber	1.33–1.39	X-pol	1506	30,000	3.33×10^{-6}	6.64×10^{-6}
[7]	Internal metal coated PCF SPR sensor	1.33–142	Y-pol	1420	11,000	9.1×10^{-6}	7.04×10^{-6}
[38]	Circularly slotted highly sensitive	1.40–1.46	N/A	780	16,000	6.25×10^{-6}	1.28×10^{-6}
[39]	Multi-coating PCF SPR at near-infrared wavelength	1.40–1.44	N/A	1739.26	9600	1.04×10^{-6}	5.77×10^{-6}
[40]	Hollow core circular shaped PCF biosensor	1.33–1.42	N/A	2456	21,000	4.76×10^{-6}	4.07×10^{-6}
[7]	Selectively coated photonic crysta	1.33–1.41	N/A	2843	18,000	5.6×10^{-6}	3.5×10^{-6}
[33]	Dual-polarized highly sensitive	1.33–1.4	N/A	1189.5	13,000	7.69×10^{-6}	8.41×10^{-6}
Proposed Sensor	Gold coated Circular PCF SPR sensor	1.35–1.41	Y-pol	4738.9	8000 14,500(X-pol)	1.25×10^{-5} 6.9×10^{-6}	2.11×10^{-6}

1.41 for the analyte refractive index (RI). FOM values of 387 and 364 are obtained for x and y polarization respectively. The lowest wavelength sensor resolution offered by this sensor is 6.9×10^{-6} RIU/nm. With existing advances, the manufacture of the sensor can be acknowledged directly alongside basic handy use. With existing technologies, the fabrication of the sensor can be realized straightforwardly along with simple practical utilization. Having such striking identifying properties, the proposed sensor has brilliant potential in the field of biomedicine, science and for error-free and exact identification of other natural and biomedical applications.

References

1. A.A. Rifat et al., Surface plasmon resonance photonic crystal fiber biosensor: a practical sensing approach. IEEE Photonics Technol Lett **27**(15), 1628–1631 (2015)
2. S.W. James, R.P. Tatam, Optical fibre long-period grating sensors: characteristics and application. Meas Sci Technol **14**, R49 (2003)
3. B. Liedberg, C. Nylander, I. Lunstrom, Surface plasmon resonance for gas detection and biosensing. Sens Actuators **4**, 299–304 (1983)
4. Y. Zhao, Z.-Q. Deng, J. Li, Photonic crystal fiber based surface plasmon resonance chemical sensors. Sens Actuators B **202**, 557–567 (2014)
5. B.D. Gupta, Surface plasmon resonance based fiber optic sensors. Rev Plasmonic **10**, 105–137 (2012)
6. W.J. Bender, R.E. Dessy, *Surface Plasmon Resonance Sensor* (Google Patents, USA, 1994).
7. A.A. Rifat, R. Ahmed, G.A. Mahdiraji, F.M. Adikan, A.E. Miroshnichenko, Highly sensitive selectively coated photonic crystal fiber-based plasmonic sensor. Opt Lett **43**, 891–894 (2018)
8. J. Homola, Present and future of surface plasmon resonance biosensors. Anal Bioanal Chem **377**, 528–539 (2003)
9. A. Rifat, G. Mahdiraji, D. Chow, Y. Shee, R. Ahmed, F. Adikan, Photonic crystal fiber-based surface plasmon resonance sensor with selective analyte channels and graphene-silver deposited core. Sensors **15**, 11499–11510 (2015)
10. M.A. Schmidt, L.P. Sempere, H.K. Tyagi, C.G. Poulton, P.S.J. Russell, Waveguiding and plasmon resonances in two-dimensional photonic lattices of gold and silver nanowires. Phys Rev B **77**, 033417 (2008)
11. F. Haider, R.A. Aoni, Md. Rajib Ahmed, S. Islam, A.E. Miroshnichenko, Propagation controlled photonic crystal fiber based plasmonic sensor via scaled-down approach. IEEE Sensors J **99**, 11 (2018)
12. R. Otupiri, E. Akowuah, S. Haxha, H. Ademgil, F. AbdelMalek, A. Aggoun, A Novel birefrigent photonic crystal fibre surface plasmon resonance biosensor. IEEE Photonic J **6**, 4 (2014)
13. ME Rahaman, R Saha, MS Ahsan, I-B Sohn (2018) Design and performance analysis of a D-shaped PCF and surface plasmon resonance based glucose sensor. International Conference on Electrical Engineering and Information and Communication Technology (ICEEICT), Bangladesh
14. T. Huang, Highly sensitive SPR sensor based on D-shaped photonic crystal fiber coated with Indium Tin Oxide at near-infrared wavelength. Plasmonics **12**(3), 123 (2017)
15. C. Liu, L. Yang, X. Lu, Q. Liu, F. Wang, J. Lv, T. Sun, H. Mu, P.K. Chu, Mid-infrared surface plasmon resonance sensor based on photonic crystal fibers. Opt Express **25**, 14227–14237 (2017)
16. Q. Liu, S. Li, H. Chen, J. Li, Z. Fan, High-sensitivity plasmonic temperature sensor based on photonic crystal biosensor based on surface plasmon resonance. Appl Opt **57**, 1883–1886 (2018)
17. R. Zakaria, W. Kam, Y.S. Ong, S.F.A.Z. Yusoff, H. Ahmad, W.S. Mohammed, Fabrication and simulation studies on D-shaped optical fiber sensor via surface plasmon resonance. J Modern Optics **64**(14), 1443–1449 (2017)
18. A.A. Rifat, R. Ahmed, G.A. Mahdiraji, F.R.M. Adikan, Highly sensitive D-shaped photonic crystal fiber-based plasmonic biosensor in visible to near-IR. IEEE Sens J **17**(9), 2776–2783 (2017)
19. R. Jha, J. Dash, Graphene based birefringent photonic crystal fiber sensor using surface plasmon resonance. IEEE PhotonTech L **26**, 1092–1095 (2014)

20. M.A. Mahfuz, M.A. Mollah, M.R. Momota, A.K. Paul, A. Masud, S. Akter, M.R. Hasan, Highly sensitive photonic crystal fiber plasmonic sensor: design and analysis. Opt Mater **90**, 315–321 (2019)
21. Md.S. Islam, C.M.B. Cordeiro, J. Sultana, R.A. Aoni, S. Feng, R. Ahmed, M. Dorraki, A. Dinovitser, B.W.-H. Ng, D. Abbott, A Hi-Bi ultra-sensitive surface plasmon resonance fiber sensor. IEEE Access **7**, 79085–79094 (2019)
22. S. Islam, J. Sultana, R.A. Aoni, S. Habib, A. Dinovitser, B.-H. Ng, D. Abbott, Localized surface plasmon resonance biosensor: an improved technique for SERS response intensification. Optics Lett **44**, 5 (2019)
23. M.R. Islam, Md. Abu Jamil, Md. Siraz-Uz Zaman, S.A.H. Ahsan, M.K. Pulak, Md. Fariha Mehjabin, M.I. Khan, J.A. Chowdhury, M. Islam, Design and analysis of birefringent SPR based PCF biosensor with ultra-high sensitivity and low loss. Optik **221**, 134–245 (2020)
24. M.S. Aruna Gandhi, K. Senthilnathan, P.R. Babu, Q. Li, Visible to near infrared highly sensitive microbiosensor based on surface plasmon polariton with external sensing approach. Results Physics **15**, 8 (2019)
25. F. Haider, R.A. Aoni, R. Ahmed, A.E. Miroshnichenko, Highly amplitude-sensitive photonic-crystal-fiber-based plasmonic sensor. J Opt Soc Am B **35**, 2816–2821 (2018)
26. A. Shafkat, Analysis of a gold coated plasmonic sensor based on a duplex core photonic crystal fiber. Sens Bio-Sens Res **28**, 6 (2020)
27. M.S. Hoseinian, M.A. Bolorizadeh, Design and simulation of a highly sensitive spr optical fiber sensor. Photonic Sens **9**, 33–42 (2019)
28. F. Mohr, *Gold Chemistry: Applications and Future Directions in the Life Sciences* (Wiley, New York, USA, 2009).
29. M.M. Rahman, M.M. Rana, M.S. Anower et al., Design and analysis of photonic crystal fiber-based plasmonic microbiosensor: an external sensing scheme. SN Appl Sci **2**, 1194 (2020)
30. M. Mahfuz, M. Mollah, M. Momota et al., Highly sensitive photonic crystal fiber plasmonic biosensor: design and analysis. Optical Mater **90**, 4 (2019)
31. K. Sharma, R. Jha, B.D. Gupta, Fiber-optic sensors based on surface plasmon resonance: a comprehensive review. IEEE Sensors J **7**(8), 1118–1129 (2007)
32. M. Rakibul Islam, M. Khan, F. Mehjabin et al., Design of a fabrication friendly and highly sensitive surface plasmon resonance-based photonic crystal fiber biosensor. Result Physics **19**, 122–234 (2020)
33. M.R. Islam, A.N.M. Iftekher, K.R. Hasan, Md. Julkar Nayen, S.B. Islam, Dual-polarized highly sensitive surface-plasmon-resonance-based chemical and biomolecular sensor. Appl Opt **59**, 3296–3305 (2020)
34. M.R. Hasan, S. Akter, A.A. Rifat, S. Rana, K. Ahmed, R. Ahmed, H. Subbaraman, D. Abbott, Spiral photonic crystal fiber-based dual-polarized surface plasmon resonance biosensor. IEEE Sens **18**, 133–140 (2018)
35. E. Haque, M.A. Hossain, F. Ahmed, Y. Namihira, Surface plasmon resonance sensor based on modified D -shaped photonic crystal fiber for wider range of refractive index detection. IEEE Sensors J **18**(20), 8287–8293 (2018)
36. https://www.rp-photonics.com/optical_spectrum_analyzers.html.
37. F. Haider, R.A. Aoni, R. Ahmed, M.S. Islam, A.E. Miroshnichenko, Propagation controlled photonic crystal fiber-based plasmonic sensor via scaled-down approach. IEEE Sensors J **19**(3), 962–969 (2019)
38. Md. Nazmus Sakib, S.M. Riazul Islam, T.V. Mahendiran, L.F. Abdulrazak, Md. Shofiqul Islam, I.M. Mehedi, Q.M. Kamrunnahar, Md. Maliha Momtaj, I.S. Walid Hassan, Md. Amiri, B. Hossain, Numerical study of circularly slotted highly sensitive plasmonic biosensor: a novel approach. Results Physics **1**, 17 (2020)
39. D. Li, W. Zhang, H. Liu, J. Hu, G. Zhou, High sensitivity refractive index sensor based on multicoating photonic crystal fiber with surface plasmon resonance at near-infrared wavelength. IEEE Photonics J **9**, 1–8 (2017)
40. Md. Biplob Hossain, S.M. Riazul Islam, K.M. Tasrif Hossain, L.F. Abdulrazak, Md. Nazmus Sakib, I.S. Amiri, High sensitivity hollow core circular shaped PCF surface plasmonic biosensor employing silver coat: a numerical design and analysis with external sensing approach. Results Physics **16**, 1 (2020)

Terms and Conditions

Springer Nature journal content, brought to you courtesy of Springer Nature Customer Service Center GmbH (“Springer Nature”).
Springer Nature supports a reasonable amount of sharing of research papers by authors, subscribers and authorised users (“Users”), for small-scale personal, non-commercial use provided that all copyright, trade and service marks and other proprietary notices are maintained. By accessing, sharing, receiving or otherwise using the Springer Nature journal content you agree to these terms of use (“Terms”). For these purposes, Springer Nature considers academic use (by researchers and students) to be non-commercial.
These Terms are supplementary and will apply in addition to any applicable website terms and conditions, a relevant site licence or a personal subscription. These Terms will prevail over any conflict or ambiguity with regards to the relevant terms, a site licence or a personal subscription (to the extent of the conflict or ambiguity only). For Creative Commons-licensed articles, the terms of the Creative Commons license used will apply.
We collect and use personal data to provide access to the Springer Nature journal content. We may also use these personal data internally within ResearchGate and Springer Nature and as agreed share it, in an anonymised way, for purposes of tracking, analysis and reporting. We will not otherwise disclose your personal data outside the ResearchGate or the Springer Nature group of companies unless we have your permission as detailed in the Privacy Policy.
While Users may use the Springer Nature journal content for small scale, personal non-commercial use, it is important to note that Users may not:

1. use such content for the purpose of providing other users with access on a regular or large scale basis or as a means to circumvent access control;
2. use such content where to do so would be considered a criminal or statutory offence in any jurisdiction, or gives rise to civil liability, or is otherwise unlawful;
3. falsely or misleadingly imply or suggest endorsement, approval , sponsorship, or association unless explicitly agreed to by Springer Nature in writing;
4. use bots or other automated methods to access the content or redirect messages
5. override any security feature or exclusionary protocol; or
6. share the content in order to create substitute for Springer Nature products or services or a systematic database of Springer Nature journal content.

In line with the restriction against commercial use, Springer Nature does not permit the creation of a product or service that creates revenue, royalties, rent or income from our content or its inclusion as part of a paid for service or for other commercial gain. Springer Nature journal content cannot be used for inter-library loans and librarians may not upload Springer Nature journal content on a large scale into their, or any other, institutional repository.
These terms of use are reviewed regularly and may be amended at any time. Springer Nature is not obligated to publish any information or content on this website and may remove it or features or functionality at our sole discretion, at any time with or without notice. Springer Nature may revoke this licence to you at any time and remove access to any copies of the Springer Nature journal content which have been saved.
To the fullest extent permitted by law, Springer Nature makes no warranties, representations or guarantees to Users, either express or implied with respect to the Springer nature journal content and all parties disclaim and waive any implied warranties or warranties imposed by law, including merchantability or fitness for any particular purpose.
Please note that these rights do not automatically extend to content, data or other material published by Springer Nature that may be licensed from third parties.
If you would like to use or distribute our Springer Nature journal content to a wider audience or on a regular basis or in any other manner not expressly permitted by these Terms, please contact Springer Nature at

onlineservice@springernature.com